The Smithian-Spathian boundary: a critical juncture in the Early Triassic recovery of marine ecosystems.

Thomas J. Algeo, Arnaud Brayard, Sylvain Richoz

The Smithian-Spathian boundary: A critical juncture in the Early Triassic recovery of marine ecosystems

1. Introduction

The Smithian-Spathian boundary (SSB), i.e., the transition between the Smithian and Spathian substages of the Olenekian Stage (late Early Triassic), represents a key interval associated with some of the most profound climatic, oceanic, and biotic changes of the Early Triassic. The SSB marked a shift away from the extreme fluctuating global environmental conditions that followed the end-Permian crisis (i.e., during the Griesbachian-Smithian substages) to potentially less severe conditions during the latter part of the Early Triassic (i.e., the Spathian substage). At the SSB, a major cooling event was accompanied by re-invigorated global-ocean circulation and turnovers in a number of marine invertebrate clades. The present thematic issue explores these developments in a series of 11 studies covering aspects of the biostratigraphy, paleoecology, paleoceanography, and volcanic history of the late Early Triassic, with special emphasis on the SSB.

2. Biostratigraphy and paleoecology of Smithian-Spathian transition

The Early Triassic comprises two official stages, the Induan and Olenekian, with the latter divided into two substages, the Smithian and Spathian (Fig. 1). Although formal definition of the Induan and Olenekian stages is underway (www.stratigraphy.org/index.php/ics-gssps), the International Commission on Stratigraphy (ICS)'s Subcommission on Triassic Stratigraphy (STS) has not yet begun to consider substage boundaries in detail. With regard to the SSB, this situation is inconvenient as geochemical and paleobiological studies of this boundary have advanced rapidly, showing major concomitant biotic and abiotic events, as reflected in the contributions to the present thematic issue, accentuating the need for formal definition of the boundary. Inconsistent placement of the SSB in different sections to date has led to conflicting interpretations of Smithian-Spathian transition events (e.g., Sun et al., 2012, 2013; Goudemand et al., 2013). Another pressing issue is refinement of Early Triassic geochronology. At present, the durations of the Early Triassic substages remain contentious, with two competing and largely irreconcilable age models in use: one based on zircon U-Pb dating that has assigned durations of ~0.7 Myr to the Smithian and ~3.0 Myr to the Spathian (Ovtcharova et al., 2006; Lehrmann et al., 2006; Galfetti et al., 2007; Mundil et al., 2010; Baresel et al., 2017), and one based on cyclostratigraphic analysis of continental redbed successions in Germany and marine successions in China that has assigned durations of ~1.7 Myr to the Smithian and ~1.4 Myr to the Spathian (Szurlies, 2007; Li et al., 2016; Ogg et al., 2016). Resolution of these issues would establish a more robust biostratigraphic-geochronologic framework for future studies of the late Early Triassic.

In this volume, **Zhang-L et al. (2019a)** review the historical foundations of the Smithian and Spathian substages, survey ammonoid and conodont biostratigraphic studies on a regional basis, and evaluate chemostratigraphic (especially carbon isotope) records for the SSB, with the overarching goal of laying the groundwork for a formal definition of the SSB in the future. This

study shows that viable definitions must take into consideration key changes in ammonoid faunas (e.g., from *Wasatchites*, *Anasibirites*, *Glyptophiceras* and *Xenoceltites* in the late Smithian to *Bajarunia*, *Tirolites* and *Columbites* in the early Spathian) and conodont faunas (e.g., *Scythogondolella milleri, Novispathodus waageni*, and *Borinella buurensis* in the late Smithian to *'Triassospathodus' hungaricus*, *Neogondolella* aff. *sweeti,* and *Icriospathodus* spp. in the early Spathian). It also reviews recent debate concerning suitability of the conodont *Novispathodus pingdingshanensis* as a potential SSB marker and its possible diachronous first occurrence, as well as the utility of the N3-to-P3 carbonate $\delta^{13}C$ shift (note: numbering system of Song et al., 2013, 2014) to constrain the position of the SSB in sections without adequate biostratigraphic control. Finally, this study evaluates inconsistencies in placement of the SSB in earlier studies, which has led to some confusion about the basic nature of paleoclimatic and oceanographic changes during the Smithian-Spathian transition. Specifically, it shows that Early Triassic hyperwarming peaked around the middle/late Smithian boundary (i.e., Smithian Thermal Maximum, or STM) and not at the SSB itself, as proposed in some earlier studies, and that the SSB coincided with a major cooling episode.

Correlations of Early Triassic conodont assemblages can be difficult owing to a high degree of endemism and some uncertainties in taxonomic determination (Krystyn et al., 2007; Zhao et al., 2007, 2013; Chen et al., 2015, 2016; Guex et al., 2015; Henderson, 2018). In this volume, **Chen et al. (2019)** use a combination of paleontological and geochemical methods to establish a high-resolution biostratigraphy based on 7 conodont Unitary Association zones (UAZs; Guex and Davaud, 1984) for the Smithian-Spathian boundary interval for two sections in Oman. Earlier studies have defined conodont UAZs for the Permian-Triassic transition (Brosse et al., 2016). In their study, Chen et al. (2019) extend UAZs into the mid-Spathian. In combination with previously published data from both South-Central Europe and South China, they identify the Smithian-Spathian boundary in the interval from UAZ4 to UAZ5, close to the last occurrence of *Nv. pingdingshanensis* in Oman and South China, and within the range of *P. inclinata*, *Ns. planus*, *Pl. regularis*, and *Pl. corniger* in south-central Europe. The UAZ7 fauna displays a clear diachronism, originating in South China and arriving progressively later in Oman and the western Tethys. Thus, this study provides insights into the challenges of working with Early Triassic conodont assemblages and the utility of UAZs in refining Early Triassic biostratigraphic zonations and identifying faunal migration patterns.

Changes in faunal size are common during intervals of environmental disturbance. Decreases in size are particularly reported, and this phenomenon has been designated the "Lilliput Effect" (Urbanek et al., 1993). It has been documented among various marine invertebrate clades in the aftermath of the severe mass extinctions at the Permian-Triassic boundary (Twitchett, 2007; Song et al., 2011; Chen et al., 2013; Chu et al., 2015) and the Cretaceous-Paleogene boundary (Keller and Abramovich, 2009; Tantawy et al., 2009), although the reality of the Lilliput Effect has engendered debate (Brayard et al., 2010, 2015; Fraiser et al., 2011). In this volume, **Leu et al. (2019)** investigate changes in the size of P1 elements of different conodont clades during the SSB transition. Assuming positive scaling between P1 elements and body size, they infer size decreases among segminate conodonts and concurrent size increases among segminiplanate conodonts during the extreme conditions of the STM, thus demonstrating that such responses to environmental perturbations can be clade-specific and that a simple general relationship between temperature and size cannot be formulated.

Segminiplanate conodonts exhibit an increase in size across the SSB, accompanying the sharp cooling (Sun et al., 2012; Romano et al., 2013)), but this increase continued during the general amelioration of oceanic environmental conditions of the early Spathian (Zhang-L et al., 2015; Song et al., 2019), indicating that temperature alone cannot explain size variations of this clade .

3. Chemostratigraphy of Smithian-Spathian transition

The oceans of the Early Triassic experienced multiple major perturbations as shown by proxy records for paleotemperatures (Sun et al., 2012; Romano et al., 2013), the carbon cycle (e.g., Payne et al., 2004; Tong et al., 2007), water-column stratification (Song et al., 2013), seawater pH (Hinojosa et al., 2012; Clarkson et al., 2015), redox conditions (Lau et al., 2016; Elrick et al., 2017), and unusual carbonate precipitates (Baud et al., 2007; Tian et al., 2015). The marine sulfur cycle was significantly perturbed during the Early Triassic as well, as reflected in strongly fluctuating $\delta^{34}S$ profiles in carbonate-associated sulfate (CAS) (e.g., Song et al., 2014). Oceanic environmental perturbations during the Early Triassic generally, and at the SSB specifically, are likely to have been a primary factor in wide biodiversity fluctuations among ammonoids, conodonts, and other marine invertebrate clades (Brayard et al., 2006, 2009; Orchard, 2007; Stanley, 2009; Wignall et al., 2016).

This volume contains several high-resolution case studies of $\delta^{34}S_{CAS}$ variation in SSB sections representing different ocean basins. **Stebbins et al. (2019a)** examine $\delta^{34}S_{CAS}$, $\delta^{18}O_{CAS}$, and $\delta^{34}S_{pyrite}$ variation in the Jesmond section (Cache Creek Terrane, western Canada), representing a carbonate atoll in the central Panthalassic Ocean, which comprised about 85% of the Early Triassic global ocean. All profiles, which span the late Smithian to mid-Spathian, show increases across the SSB, paralleling trends in $\delta^{13}C_{carb}$, that are interpreted to record a global increase in microbial sulfate reduction (MSR) and pyrite burial. A decrease immediately following the SSB indicates that these environmental changes reached maxima and began to diminish or reverse in the early Spathian. Based on the "MSR-trend" method of Algeo et al. (2015), differences between paired $\delta^{34}S_{CAS}$ and $\delta^{34}S_{pyr}$ values ($\Delta^{34}S_{CAS\text{-}pyr}$) yield estimates of SSB seawater sulfate concentrations between 2.5 and 9.1 mM. These estimates are higher than previous estimates for the PTB (<4 mM; Luo et al., 2010; Song et al., 2014), suggesting an increase in seawater sulfate following a minimum around the Permian-Triassic boundary.

In a second study, **Stebbins et al. (2019b)** examine $\delta^{34}S_{CAS}$, $\delta^{18}O_{CAS}$, and $\delta^{34}S_{pyrite}$ variation in the Mud section (Spiti Valley, northern India), representing a mixed siliciclastic-carbonate shelf on the southern margin of the Neotethys Ocean. This section, which spans the mid-Griesbachian to mid-Spathian, exhibits secular excursions that are consistent in timing and magnitude with those previously documented from South China (Song et al., 2014), demonstrating that CAS is a robust recorder of a global seawater sulfate signal. Peak CAS and pyrite $\delta^{34}S$ values, representing maximum rates of MSR and pyrite burial, coincided with intervals of relatively cooler sea-surface temperatures. The authors infer that episodes of climatic cooling during the Early Triassic, especially at the SSB but also near the Griesbachian-Dienerian and Dienerian-Smithian boundaries, led to steepened equator-to-pole temperature gradients (Brayard et al., 2006), invigorating thermohaline overturning circulation (cf. Clarkson et al., 2016; Huang et al., 2017), and enhancing upwelling of nutrients that stimulated marine

productivity and increased organic carbon sinking fluxes. Enhanced productivity fueled oceanic euxinia, primarily within thermoclinal oxygen-minimum zones (Algeo et al., 2011a; Winguth and Winguth, 2012), leading to increased burial of ^{34}S-depleted pyrite and ^{34}S- and ^{18}O-enrichment of the oceanic sulfate pool. This study also documents a slow increase in $\Delta^{34}S_{CAS\text{-}pyr}$ through the Early Triassic due to a slow rise in seawater sulfate concentrations, confirming the inference of Stebbins et al. (2019a).

Also in this volume, **Thomazo et al. (2019)** analyze multiple sulfur isotopes (^{32}S, ^{33}S, ^{34}S, and ^{36}S) of sedimentary pyrite and CAS from the Mineral Mountains section, Utah, a shallow carbonate shelf on the eastern margin of the Early Triassic Panthalassic Ocean. This section, spanning the Smithian to lower Spathian, exhibits strong $\delta^{34}S_{pyrite}$ variation accompanied by limited $\delta^{34}S_{CAS}$ variation (+19.5 ‰ to +34.8 ‰) and $\Delta^{33}S_{pyrite}$ values of −0.01 ‰ to +0.12 ‰ as evidence of the operation of porewater synsedimentary microbial sulfate reduction in an open (sulfate-unlimited) system before the late Smithian, evolving to a closed (sulfate-limited) system at the SSB in response to local sedimentological controls (e.g., bioturbation intensity and sedimentation rate), rather than as a consequence of development of widespread marine anoxia in the Early Triassic global ocean.

The marine sulfur and carbon cycles were closely coupled during much of the Early Triassic. Marine carbonate carbon isotope records exhibit large fluctuations (to 5-10 ‰), especially during the Griesbachian to Smithian substages, followed by more muted changes during the Spathian substage (e.g., Payne et al., 2004; Tong et al., 2007; Richoz et al., 2010). Multiple scenarios have been proposed to account for these carbon cycle perturbations, including volcanic emissions (Payne and Kump, 2007), soil organic matter inputs (Sephton et al., 2005), marine productivity changes (Meyer et al., 2011), or combinations of these factors (Algeo et al., 2011b). In this volume, **Lyu et al. (2019)** examine changes in marine carbonate $\delta^{13}C$ records at West Pingdingshan and Jiarong in South China during the S-S transition, documenting shifts up to 5-10 ‰ in multiple widely separated sections. The large positive $\delta^{13}C_{carb}$ shift at the SSB has been attributed to increased marine productivity as a result of intensified upwelling (Song et al., 2014; Zhang-L et al., 2015). Increased upwelling is consistent with invigorated oceanic circulation and weakened oceanic stratification, which is reflected in reduced vertical $\delta^{13}C_{DIC}$ gradients (Song et al., 2013) and increases in extended tricyclic terpanes (ETR; Saito et al., 2013). These oceanic developments at the SSB may have been triggered by cooling following the STM (Zhang-L et al., 2019).

In this volume, **Song et al. (2019)** investigate redox changes in a paleo-upwelling zone on the paleo-western margin of the South China Craton during the SSB transition, based on analysis of carbon-sulfur-iron (C-S-Fe) systematics in the South Majiashan section. This section exhibits a transient anoxic event concurrently with rapid positive shifts in $\delta^{13}C_{carb}$ and $\delta^{34}S_{CAS}$ across the SSB, which is interpreted as a signature of enhanced marine productivity in response to intensified upwelling. This scenario accords with inferences developed in all of the studies cited above, in which the SSB transition marks an interval of rapid cooling and re-invigoration of global-ocean overturning circulation and upwelling on continental margins. This cooling event bookmarks the termination of the STM and initiates an extended interval of ameliorated climatic and oceanic environmental conditions during the Spathian substage. The study of Song et al. (2019) specifically links enhanced burial of organic carbon to the cooling trend that developed around the SSB, and proposes that a positive feedback between cooling and

enhanced oceanic circulation existed until all of the nutrients that had accumulated in the deep ocean during its stagnant phase (i.e., Griesbachian-Smithian substages) had been flushed out.

4. Global events during the Smithian-Spathian transition

Until recently, analysis of redox conditions in paleomarine systems was based exclusively on proxies that provided information about local conditions, requiring many such studies to evaluate whole-ocean redox changes through time. The U-isotopic composition of marine carbonates now permits rapid assessment of global-ocean redox changes through time, as shown by numerous studies of the PTB (e.g., Brennecka et al., 2011a; Lau et al., 2016; Elrick et al., 2017; Zhang-F et al., 2018a, 2018b) and other geologic intervals (e.g., Dahl et al., 2014; White et al., 2018). Although some of the earlier PTB studies extended their analysis into or through the Early Triassic, none covered the Smithian-Spathian transition at the high level of stratigraphic resolution of **Zhang-F et al. (2019)** in this volume. In this study, carbonate U-isotope profiles were generated for two sections, one representing an atoll in the central Panthalassic Ocean (Jesmond) and the other a platform in the eastern Paleotethys Ocean (Zuodeng), in order to constrain variations in oceanic anoxia and its links to biotic and climatic changes during the Smithian-Spathian transition. These two sections yielded identical secular patterns, demonstrating that they record a global signal, which is characterized by a minimum in the late Smithian (–0.6 to –0.7 ‰) followed by a rapid positive shift across the SSB (to ~0 ‰) and a shift back to more negative values (–0.4 to –0.6 ‰) in the early to middle Spathian. Based on mass balance modeling, these values correspond to changes in the global area of anoxic seafloor from a peak of ~11 % in the late Smithian (i.e., coincident with the STM; Zhang-L et al., 2019) to a minimum of ~2 % in the early Spathian (i.e., during the post-SSB cool interval).

During the STM, Early Triassic tropical sea-surface temperatures (SSTs) reached their peak of ~40 °C, followed by a decline to somewhat lower temperatures (~32 °C) by the early Spathian, as revealed by conodont $\delta^{18}O$ records (Fig. 1A) (Sun et al., 2012; Romano et al., 2013). The SSB cooling event was accompanied by a steepening of the latitudinal temperature gradient, as reflected in ammonoid faunal distributions (Brayard et al., 2006). In this volume, **Goudemand et al. (2019)** examine temperature trends during the Smithian-Spathian transition based on new conodont $\delta^{18}O$ data. They present a high-resolution record from the Salt Range (Pakistan), documenting in greater detail the major cooling event that occurred during the SSB transition. These results imply that climatic cooling was an important factor in the recovery of marine biotas during the early Spathian (e.g., Brayard et al., 2006, 2009, 2017; Stanley, 2009; Brosse et al., 2013).

The ultimate cause of global climatic cooling and attendant changes in oceanic circulation during the SSB transition is uncertain. Links to Siberian Traps Large Igneous Province (STLIP) activity have been speculated upon, but without much firm evidence to date. Sedimentary mercury (Hg) enrichments have recently emerged as a proxy for volcanic inputs to sedimentary successions, potentially providing information about the intensity, duration, and episodicity of volcanic activity (Sanei et al., 2012; Font et al., 2016; Thibodeau et al., 2016). The residence time of Hg in the atmosphere is sufficiently long to ensure that volcanic Hg is distributed widely following major eruptive events but sufficiently short to ensure its rapid removal to the sediment, resulting in discrete Hg-rich event horizons. In this volume, **Shen et al.**

(2019) use Hg concentrations to examine the record of volcanism through the Early Triassic, with a focus on the SSB, based on five sections from the Paleotethys, Neotethys, and Panthalassic oceans. Their results show that volcanic activity was nearly continuous through the first ~1.3 Myr of the Early Triassic at a global scale, probably related to emissions from the STLIP, and that the level of volcanic activity plunged sharply at the SSB. This event may have been a primary cause of climatic cooling at the SSB (Sun et al., 2012; Romano et al., 2013) as well as of reduced continental weathering rates as revealed by stabilization of seawater $^{87}Sr/^{86}Sr$ values (Sedlacek et al., 2014). This study thus provides direct evidence of a close link between volcanism and climatic-oceanic perturbations of the Early Triassic, and that the amelioration of environmental conditions and accelerated recovery of marine ecosystems during the Spathian were potentially tied to a decline in volcanic activity.

5. Concluding remarks

The present thematic issue contains 11 studies presenting a combination of new research and reviews on aspects of the biostratigraphy, paleoecology, paleoceanography, and volcanism during the transition between the Smithian and Spathian substages of the Early Triassic. The SSB was a key interval associated with major climatic, oceanic and biotic changes of the Early Triassic, coinciding with the first sustained amelioration of environmental conditions and recovery of marine ecosystems following the end-Permian crisis. These studies represent the current state of knowledge regarding the SSB event and lay the groundwork for future studies on this topic.

References

Algeo, T.J., Kuwahara, K., Sano, H., Bates, S., Lyons, T., Elswick, E., Hinnov, L., Ellwood, B., Moser, J., Maynard, J.B., 2011a. Spatial variation in sediment fluxes, redox conditions, and productivity in the Permian–Triassic Panthalassic Ocean. Palaeogeography, Palaeoclimatology, Palaeoecology 308(1-2), 65-83.

Algeo, T.J., Chen, Z.Q., Fraiser, M.L., Twitchett, R.J., 2011b. Terrestrial–marine teleconnections in the collapse and rebuilding of Early Triassic marine ecosystems. Palaeogeography, Palaeoclimatology, Palaeoecology 308(1-2), 1-11.

Algeo, T.J., Henderson, C.M., Tong, J., Feng, Q., Yin, H., Tyson, R.V., 2013. Plankton and productivity during the Permian–Triassic boundary crisis: an analysis of organic carbon fluxes. Global and Planetary Change 105, 52-67.

Algeo, T.J., Luo, G.M., Song, H.Y., Lyons, T.W., Canfield, D.E., 2015. Reconstruction of secular variation in seawater sulfate concentrations. Biogeosciences 12(7), 2131-2151.

Baresel, B., Bucher, H., Brosse, M., Cordey, F., Guodun, K., Schaltegger, U., 2017. Precise age for the Permian–Triassic boundary in South China from high-precision U-Pb geochronology and Bayesian age–depth modeling. Solid Earth 8(2), 361-378.

Baud, A., Richoz, S., Pruss, S., 2007. The lower Triassic anachronistic carbonate facies in space and time. Global and Planetary Change 55(1-3), 81-89.

Brayard, A., Bucher, H., Escarguel, G., Fluteau, F., Bourquin, S., Galfetti, T., 2006. The Early Triassic ammonoid recovery: paleoclimatic significance of diversity gradients. Palaeogeography, Palaeoclimatology, Palaeoecology 239(3-4), 374-395.

Brayard, A., Escarguel, G., Bucher, H., Brühwiler, T., 2009. Smithian and Spathian (Early Triassic) ammonoid assemblages from terranes: paleoceanographic and paleogeographic implications. Journal of Asian Earth Sciences 36(6), 420-433.

Brayard, A., Nützel, A., Stephen, D.A., Bylund, K.G., Jenks, J., Bucher, H., 2010. Gastropod evidence against the Early Triassic Lilliput effect. Geology 38(2), 147-150.

Brayard, A., Meier, M., Escarguel, G., Fara, E., Nützel, A., Olivier, N., Bylund, K.G., Jenks, J.F., Stephen, D.A., Hautmann, M., Vennin, E., Bucher, H., 2015. Early Triassic Gulliver gastropods: Spatio-temporal distribution and significance for biotic recovery after the end-Permian mass extinction. Earth-Science Reviews 146, 31-64.

Brayard, A., Krumenacker, L.J., Botting, J.P., Jenks, J.F., Bylund, K.G., Fara, E., Vennin, E., Olivier, N., Goudemand, N., Saucède, T., Charbonnier, S., 2017. Unexpected Early Triassic marine ecosystem and the rise of the Modern evolutionary fauna. Science Advances 3(2), e1602159.

Brennecka, G.A., Herrmann, A.D., Algeo, T.J., Anbar, A.D., 2011. Rapid expansion of oceanic anoxia immediately before the end-Permian mass extinction. Proceedings of the National Academy of Sciences (U.S.A.) 108(43), 17631-17634.

Brosse, M., Brayard, A., Fara, E., Neige, P., 2013. Ammonoid recovery after the Permian–Triassic mass extinction: a re-exploration of morphological and phylogenetic diversity patterns. Journal of the Geological Society of London 170(2), 225-236.

Brosse, M., Bucher, H., Goudemand, N., 2016. Quantitative biochronology of the Permian–Triassic boundary in South China based on conodont unitary associations. Earth-Science Reviews 155, 153-171.

Chen, Y.L., Twitchett, R.J., Jiang, H., Richoz, S., Lai, X., Yan, C., Sun, Y., Liu, X., Wang, L., 2013. Size variation of conodonts during the Smithian–Spathian (Early Triassic) global warming event. Geology 41(8), 823-826.

Chen, Y.L., Jiang, H.S, Richoz, S., Yan, C.B., Lai, X.L., Sun, Y.D, Liu, X.D., Wang, L.N., 2015. Early Triassic conodonts of Jiarong, Nanpanjiang Basin, southern Guizhou Province, South China. Journal of Asian Earth Sciences 105, 104-121.

Chen, Y.L., Kolar-Jurkovšek, T., Jurkovšek, B., Aljinović, D., Richoz, S., 2016. Early Triassic conodonts and carbonate carbon isotope record of the Idrija–Žiri area, Slovenia. Palaeogeography, Palaeoclimatology, Palaeoecology 444, 84-100.

Chen, Y.L., Richoz, S., Krystyn, L., Zhang, Z., 2019. Quantitative stratigraphic correlation of Tethyan conodonts across the Smithian-Spathian (Early Triassic) extinction event. Earth-Science Reviews, this volume.

Chu, D., Tong, J., Song, H.J., Benton, M.J., Song, H., Yu, J., Qiu, X., Huang, Y. and Tian, L., 2015. Lilliput effect in freshwater ostracods during the Permian–Triassic extinction. Palaeogeography, Palaeoclimatology, Palaeoecology 435, 38-52.

Clarkson, M.O., Kasemann, S.A., Wood, R.A., Lenton, T.M., Daines, S.J., Richoz, S., Ohnemueller, F., Meixner, A., Poulton, S.W., Tipper, E.T., 2015. Ocean acidification and the Permo-Triassic mass extinction. Science 348(6231), 229-232.

306 Clarkson, M.O., Wood, R.A., Poulton, S.W., Richoz, S., Newton, R.J., Kasemann, S.A., Bowyer, F.,
307 Krystyn, L., 2016. Dynamic anoxic ferruginous conditions during the end-Permian mass
308 extinction and recovery. Nature Communications 7, 12236.
309 Dahl, T.W., Boyle, R.A., Canfield, D.E., Connelly, J.N., Gill, B.C., Lenton, T.M., Bizzarro, M., 2014.
310 Uranium isotopes distinguish two geochemically distinct stages during the later Cambrian
311 SPICE event. Earth and Planetary Science Letters 401, 313-326.
312 Elrick, M., Polyak, V., Algeo, T.J., Romaniello, S., Asmerom, Y., Herrmann, A.D., Anbar, A.D.,
313 Zhao, L., Chen, Z.Q., 2017. Global-ocean redox variation during the middle-late Permian
314 through Early Triassic based on uranium isotope and Th/U trends of marine carbonates.
315 Geology 45(2), 163-166.
316 Font, E., Adatte, T., Sial, A.N., Drude de Lacerda, L., Keller, G., Punekar, J., 2016. Mercury
317 anomaly, Deccan volcanism, and the end-Cretaceous mass extinction. Geology 44(2), 171-
318 174.
319 Fraiser, M.L., Twitchett, R.J., Frederickson, J.A., Metcalfe, B., Bottjer, D.J., 2011. Gastropod
320 evidence against the Early Triassic Lilliput effect: COMMENT. Geology 39(1), e232-e232.
321 Galfetti, T., Bucher, H., Ovtcharova, M., Schaltegger, U., Brayard, A., Brühwiler, T., Goudemand,
322 N., Weissert, H., Hochuli, P.A., Cordey, F., Guodun, K., 2007. Timing of the Early Triassic
323 carbon cycle perturbations inferred from new U–Pb ages and ammonoid biochronozones.
324 Earth and Planetary Science Letters 258(3-4), 593-604.
325 Goudemand, N., Romano, C., Brayard, A., Hochuli, P.A., Bucher, H., 2013. Comment on “Lethally
326 hot temperatures during the Early Triassic greenhouse”. Science 339, p. 1033.
327 Goudemand, N., Romano, C., Leu, M., Bucher, H., Trotter, J.A., Williams, I.S., 2019. Dynamic
328 interplay between climate and marine biodiversity upheavals during the early Triassic
329 Smithian-Spathian biotic crisis. Earth-Science Reviews, this volume.
330 Guex, J., Davaud, E., 1984. Unitary associations method: use of graph theory and computer
331 algorithm. Computers & Geosciences 10(1), 69-96.
332 Guex, J., Galster, F., Hammer, Ø., 2015. Discrete Biochronological Time Scales. Springer,
333 Dordrecht, 160 pp.
334 Henderson, C.M., 2018. Permian conodont biostratigraphy. In: Lucas, S.G., Shen, S.Z. (Eds.), The
335 Permian Timescale. Geological Society of London, Special Publication 450, pp. 119-142.
336 Hinojosa, J.L., Brown, S.T., Chen, J., DePaolo, D.J., Paytan, A., Shen, S.Z., Payne, J.L., 2012.
337 Evidence for end-Permian ocean acidification from calcium isotopes in biogenic apatite.
338 Geology 40(8), 743-746.
339 Huang, Y., Chen, Z.Q., Wignall, P.B., Zhao, L., 2017. Latest Permian to Middle Triassic redox
340 condition variations in ramp settings, South China: Pyrite framboid evidence. Geological
341 Society of America Bulletin 129(1-2), 229-243.
342 Keller, G., Abramovich, S., 2009. Lilliput effect in late Maastrichtian planktic foraminifera:
343 Response to environmental stress. Palaeogeography, Palaeoclimatology, Palaeoecology
344 284(1-2), 47-62.
345 Krystyn, L., Bhargava, O.N., Richoz, S., 2007. A candidate GSSP for the base of the Olenekian
346 Stage: Mud at Pin Valley; district Lahul & Spiti, Himachal Pradesh (Western Himalaya),
347 India. Albertiana 35, 5-29.
348 Lau, K.V., Maher, K., Altiner, D., Kelley, B.M., Kump, L.R., Lehrmann, D.J., Silva-Tamayo, J.C.,
349 Weaver, K.L., Yu, M., Payne, J.L., 2016. Marine anoxia and delayed Earth system recovery

after the end-Permian extinction. Proceedings of the National Academy of Sciences (U.S.A.) 113(9), 2360-2365.
Lehrmann, D.J., Ramezani, J., Bowring, S.A., Martin, M.W., Montgomery, P., Enos, P., Payne, J.L., Orchard, M.J., Wang, H.M., Wei, J.Y., 2006. Timing of recovery from the end-Permian extinction: Geochronologic and biostratigraphic constraints from south China. Geology 34(12), 1053-1056.
Leu, M., Bucher, H., Goudemand, N., 2019. Clade-dependent size response of conodonts to environmental changes during the late Smithian extinction. Earth-Science Reviews, this volume.
Li, M., Ogg, J., Zhang, Y., Huang, C., Hinnov, L., Chen, Z.Q., Zou, Z., 2016. Astronomical tuning of the end-Permian extinction and the Early Triassic Epoch of South China and Germany. Earth and Planetary Science Letters 441, 10-25.
Luo, G., Kump, L.R., Wang, Y., Tong, J., Arthur, M.A., Yang, H., Huang, J., Yin, H., Xie, S., 2010. Isotopic evidence for an anomalously low oceanic sulfate concentration following end-Permian mass extinction. Earth and Planetary Science Letters 300(1-2), 101-111.
Lyu, Z., Zhang, L., Algeo, T.J., Zhao, L., Chen, Z.Q., Li, C., Ma, B., Ye, F., 2019. Global-ocean circulation changes during the Smithian-Spathian transition inferred from carbon-sulfur cycle records. Earth-Science Reviews, this volume.
Meyer, K.M., Yu, M., Jost, A.B., Kelley, B.M., Payne, J.L., 2011. $\delta^{13}C$ evidence that high primary productivity delayed recovery from end-Permian mass extinction. Earth and Planetary Science Letters 302(3-4), 378-384.
Mundil, R., Pálfy, J., Renne, P.R., Brack, P., 2010. The Triassic timescale: new constraints and a review of geochronological data. In: Geological Society of London, Special Publication 334, pp. 41-60.
Ogg, J.G., Ogg, G., Gradstein, F.M., 2016. A Concise Geologic Time Scale: 2016. Elsevier, Amsterdam.
Orchard, M.J., 2007. Conodont diversity and evolution through the latest Permian and Early Triassic upheavals. Palaeogeography, Palaeoclimatology, Palaeoecology 252(1-2), 93-117.
Ovtcharova, M., Bucher, H., Schaltegger, U., Galfetti, T., Brayard, A., Guex, J., 2006. New Early to Middle Triassic U–Pb ages from South China: calibration with ammonoid biochronozones and implications for the timing of the Triassic biotic recovery. Earth and Planetary Science Letters 243(3-4), 463-475.
Payne, J.L., Kump, L.R., 2007. Evidence for recurrent Early Triassic massive volcanism from quantitative interpretation of carbon isotope fluctuations. Earth and Planetary Science Letters 256(1-2), 264-277.
Payne, J.L., Lehrmann, D.J., Wei, J., Orchard, M.J., Schrag, D.P., Knoll, A.H., 2004. Large perturbations of the carbon cycle during recovery from the end-Permian extinction. Science 305(5683), 506-509.
Richoz, S., Krystyn, L., Baud, A., Brandner, R., Horacek, M., Mohtat-Aghai, P., 2010. Permian–Triassic boundary interval in the Middle East (Iran and N. Oman): Progressive environmental change from detailed carbonate carbon isotope marine curve and sedimentary evolution. Journal of Asian Earth Sciences 39(4), 236-253.

392 Romano, C., Goudemand, N., Vennemann, T.W., Ware, D., Schneebeli-Hermann, E., Hochuli,
393 P.A., Brühwiler, T., Brinkmann, W., Bucher, H., 2013. Climatic and biotic upheavals
394 following the end-Permian mass extinction. Nature Geoscience 6(1), 57-60.
395 Saito, R., Kaiho, K., Oba, M., Takahashi, S., Chen, Z.Q., Tong, J., 2013. A terrestrial vegetation
396 turnover in the middle of the Early Triassic. Global and Planetary Change 105, 152-159.
397 Sanei, H., Grasby, S.E., Beauchamp, B., 2012. Latest Permian mercury anomalies. Geology 40(1),
398 63-66.
399 Sedlacek, A.R., Saltzman, M.R., Algeo, T.J., Horacek, M., Brandner, R., Foland, K., Denniston,
400 R.F., 2014. $^{87}Sr/^{86}Sr$ stratigraphy from the Early Triassic of Zal, Iran: Linking temperature to
401 weathering rates and the tempo of ecosystem recovery. Geology 42(9), 779-782.
402 Sephton, M.A., Looy, C.V., Brinkhuis, H., Wignall, P.B., De Leeuw, J.W., Visscher, H., 2005.
403 Catastrophic soil erosion during the end-Permian biotic crisis. Geology 33(12), 941-944.
404 Shen, J., Algeo, T.J., Planavsky, N.J., Yu, J., Feng, Q., Song, H.J., Song, H.Y., Rowe, H., Zhou, L.,
405 Chen, J., 2019. Mercury enrichments provide evidence of Early Triassic volcanism following
406 the end-Permian mass extinction. Earth-Science Reviews, this volume.
407 Song, H.J., Tong, J., Chen, Z.Q., 2011. Evolutionary dynamics of the Permian–Triassic foraminifer
408 size: evidence for Lilliput effect in the end-Permian mass extinction and its aftermath.
409 Palaeogeography, Palaeoclimatology, Palaeoecology 308(1-2), 98-110.
410 Song, H.Y., Tong, J., Algeo, T.J., Horacek, M., Qiu, H., Song, H.J., Tian, L., Chen, Z.Q., 2013. Large
411 vertical $\delta^{13}C_{DIC}$ gradients in Early Triassic seas of the South China craton: Implications for
412 oceanographic changes related to Siberian Traps volcanism. Global and Planetary Change
413 105, 7-20.
414 Song, H.Y., Tong, J., Algeo, T.J., Song, H.J., Qiu, H., Zhu, Y., Tian, L., Bates, S., Lyons, T.W., Luo, G.,
415 Kump, L.R., 2014. Early Triassic seawater sulfate drawdown. Geochimica et Cosmochimica
416 Acta 128, 95-113.
417 Song, H.Y., Du, Y., Algeo, T.J., Tong, J., Owens, J.D., Song, H.J., Tian, L., Qiu, H., Zhu, Y., Lyons,
418 T.W., 2019. Cooling-driven oceanic anoxia across the Smithian/Spathian boundary (mid-
419 Early Triassic). Earth-Science Reviews, this volume.
420 Stanley, S.M., 2009. Evidence from ammonoids and conodonts for multiple Early Triassic mass
421 extinctions. Proceedings of the National Academy of Sciences (U.S.A.) 106(36), 15256-
422 15259.
423 Stebbins, A., Algeo, T.J., Olsen, C., Sano, H., Rowe, H., Hannigan, R., 2019a. Sulfur-isotope
424 evidence for recovery of seawater sulfate concentrations from a PTB minimum by the
425 Smithian-Spathian transition. Earth-Science Reviews, this volume.
426 Stebbins, A., Algeo, T.J., Krystyn, L., Rowe, H., Brookfield, M., Williams, J., Nye, S.W., Jr.,
427 Hannigan, R., 2019b. Marine sulfur cycle evidence for upwelling and eutrophic stresses
428 during Early Triassic cooling events. Earth-Science Reviews, this volume.
429 Sun, Y., Joachimski, M.M., Wignall, P.B., Yan, C., Chen, Y., Jiang, H., Wang, L., Lai, X., 2012.
430 Lethally hot temperatures during the Early Triassic greenhouse. Science 338(6105), 366-
431 370.
432 Sun, Y., Joachimski, M.M., Wignall, P.B., Yan, C., Chen, Y., Jiang, H., Wang, L., Lai, X., 2013.
433 Response to Comment on "Lethally hot temperatures during the Early Triassic
434 greenhouse". Science 339(6123), 1033-1033.

435 Szurlies, M., 2007. Latest Permian to Middle Triassic cyclo-magnetostratigraphy from the
436 Central European Basin, Germany: implications for the geomagnetic polarity timescale.
437 Earth and Planetary Science Letters 261(3-4), 602-619.
438 Tantawy, A.A.A., Keller, G., Pardo, A., 2009. Late Maastrichtian volcanism in the Indian Ocean:
439 effects on calcareous nannofossils and planktic foraminifera. Palaeogeography,
440 Palaeoclimatology, Palaeoecology 284(1), 63-87.
441 Thibodeau, A.M., Ritterbush, K., Yager, J.A., West, A.J., Ibarra, Y., Bottjer, D.J., Berelson, W.M.,
442 Bergquist, B.A., Corsetti, F.A., 2016. Mercury anomalies and the timing of biotic recovery
443 following the end-Triassic mass extinction. Nature Communications 7, 11147.
444 Thomazo, C., Brayard, A., Elmeknassi, S., Vennin, E., Olivier, N., Caravaca, G., Escarguel, G., Fara,
445 E., Bylund, K.G., Jenks, J.F., Stephen, D.A., 2019. Multiple sulfur isotope signals associated
446 with the late Smithian event and the Smithian/Spathian boundary. Earth-Science Reviews,
447 this volume.
448 Tian, L., Bottjer, D.J., Tong, J., Li, F., Yang, T., Song, H., Song, H., Liang, L., 2015. Distribution and
449 size variation of ooids in the aftermath of the Permian–Triassic mass extinction.
450 Palaios 30(9), 714-727.
451 Tong, J., Zuo, J., Chen, Z.Q., 2007. Early Triassic carbon isotope excursions from South China:
452 proxies for devastation and restoration of marine ecosystems following the end-Permian
453 mass extinction. Geological Journal 42(3-4), 371-389.
454 Twitchett, R.J., 2007. The Lilliput effect in the aftermath of the end-Permian extinction
455 event. Palaeogeography, Palaeoclimatology, Palaeoecology 252(1-2), 132-144.
456 Urbanek, A., 1993. Biotic crises in the history of Upper Silurian graptoloids: a palaeobiological
457 model. Historical Biology 7(1), 29-50.
458 White, D.A., Elrick, M., Romaniello, S., Zhang, F., 2018. Global seawater redox trends during the
459 Late Devonian mass extinction detected using U isotopes of marine limestones. Earth and
460 Planetary Science Letters 503, 68-77.
461 Wignall, P.B., Bond, D.P., Sun, Y., Grasby, S.E., Beauchamp, B., Joachimski, M.M., Blomeier, D.P.,
462 2016. Ultra-shallow-marine anoxia in an Early Triassic shallow-marine clastic ramp
463 (Spitsbergen) and the suppression of benthic radiation. Geological Magazine 153(2), 316-
464 331.
465 Winguth, C., Winguth, A.M., 2012. Simulating Permian–Triassic oceanic anoxia distribution:
466 implications for species extinction and recovery. Geology 40(2), 127-130.
467 Zhang, F., Romaniello, S.J., Algeo, T.J., Lau, K.V., Clapham, M.E., Richoz, S., Herrmann, A.D.,
468 Smith, H., Horacek, M., Anbar, A.D., 2018a. Multiple episodes of extensive marine anoxia
469 linked to global warming and continental weathering following the latest Permian mass
470 extinction. Science Advances 4(4), e1602921.
471 Zhang, F., Algeo, T.J., Romaniello, S.J., Cui, Y., Zhao, L., Chen, Z.Q., Anbar, A.D., 2018b.
472 Congruent Permian-Triassic $\delta^{238}U$ records at Panthalassic and Tethyan sites: Confirmation
473 of global-oceanic anoxia and validation of the U-isotope paleoredox proxy. Geology 46(4),
474 327-330.
475 Zhang, F., Algeo, T.J., Cui, Y., Shen, J., Song, H., Sano, H., Rowe, H.D., Anbar, A.D., 2019. Global-
476 ocean redox variations across the Smithian-Spathian boundary linked to concurrent
477 climatic and biotic changes. Earth-Science Reviews, this volume.

Zhang, L., Zhao, L., Chen, Z.Q., Algeo, T.J., Li, Y., Cao, L., 2015. Amelioration of marine environments at the Smithian–Spathian boundary, Early Triassic. Biogeosciences 12(5), 1597-1613.
Zhang, L., Orchard, M.J., Brayard, A., Algeo, T.J., Zhao, L., Chen, Z.Q., Lyu, Z., 2019. The Smithian/Spathian boundary (late Early Triassic): a review of ammonoid, conodont, and carbon-isotopic criteria. Earth-Science Reviews, this volume.
Zhao, L.S., Orchard, M.J., Tong, J.N., Sun, Z.M., Zuo, J.X., Zhang, S.X., Yun, A.L., 2007. Lower Triassic conodont sequence in Chaohu, Anhui Province, China and its global correlation. Palaeogeography, Palaeoclimatology, Palaeoecology 252, 24-38.
Zhao, L.S., Chen, Y.L., Chen, Z.Q., Cao, L., 2013. Uppermost Permian to Lower Triassic conodont zonation from Three Gorges Area, South China. Palaios 28, 523-540.

Thomas J. Algeo
Department of Geology, University of Cincinnati, Cincinnati, Ohio 45221-0013, U.S.A.
State Key Laboratory of Geological Processes and Mineral Resources, & State Key Laboratory of Biogeology and Environmental Geology, China University of Geosciences, Wuhan 430074, China
Email: thomas.algeo@uc.edu

Arnaud Brayard
Biogéosciences, UMR 6282 CNRS
Université Bourgogne Franche-Comté
21000 Dijon, France
Email: arnaud.brayard@u-bourgogne.fr

Sylvain Richoz

Department of Geology, Lund University, 22362 Lund, Sweden
Institute of Earth Sciences, NAWI Graz, Graz University, 8010 Graz, Austria
Email: sylvain.richoz@geol.lu.se

Figure caption

Fig. 1. Global paleogeography of Early Triassic (base map courtesy of Ron Blakey, Deep-Time Maps). Study sections in present volume shown in yellow; note that the paleogeographic location of Tulong is uncertain. Numbers of study sections/areas in both figures are keyed to papers in this thematic issue: (1) Zhang et al., 2019a, 2019b; (2) Chen et al., 2019; (3) Leu et al., 2019; (4) Stebbins et al., 2019a; (5) Stebbins et al., 2019b; (6) Thomazo et al., 2019; (7) Lyu et al., 2019; (8) Song et al., 2019; (9) Zhang et al., 2019a, 2019b; (10) Goudemand et al., 2019; (11) Shen et al., 2019. (For interpretation of the references to colour in this figure legend, the reader is referred to the web version of this article.)

Fig. 2. Simplified stratigraphy of Early Triassic (adapted from Algeo et al., 2013). Smithian-Spathian substages of Early Triassic shown in blue; stratigraphic ranges of studies in this volume shown by vertical bars at right, with numbers keyed as in the Fig. 1 caption. Abbreviations: LPME=latest Permian mass extinction; PTB=Permian/Triassic boundary; IOB=Induan/Olenekian boundary; SSB=Smithian/Spathian boundary; EMTB=Early/Middle Triassic boundary. (For interpretation of the references to colour in this figure legend, the reader is referred to the web version of this article.)

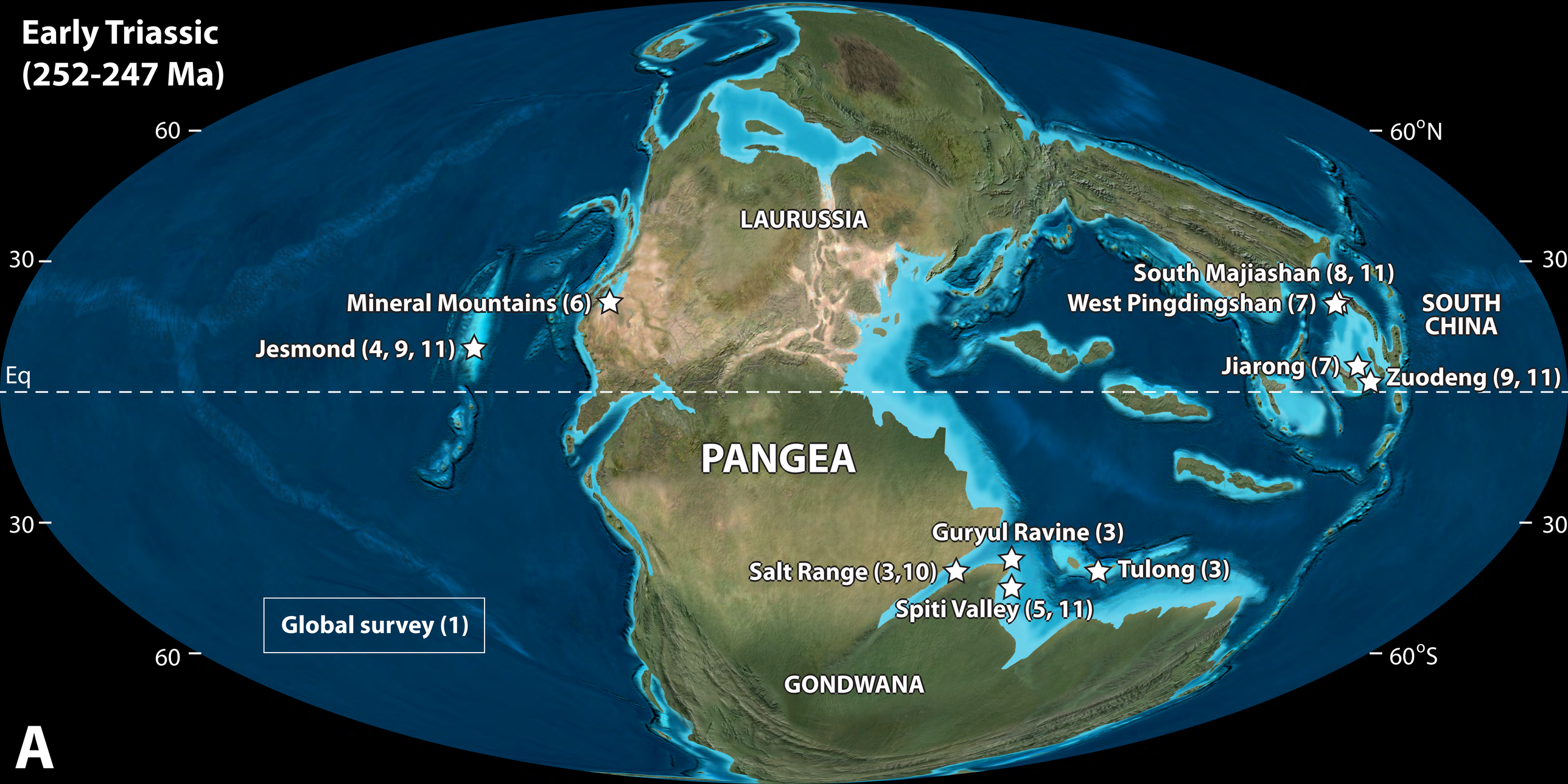
Early Triassic
(252-247 Ma)
60
60°N
30
30
LAURUSSIA
South Majiashan (8, 11)
Mineral Mountains (6)
West Pingdingshan (7)
SOUTH
CHINA
Jesmond (4, 9, 11)
Jiarong (7)
Zuodeng (9, 11)
Eq
PANGEA
30
30
Guryul Ravine (3)
Salt Range (3,10)
Tulong (3)
Spiti Valley (5, 11)
Global survey (1)
60
60°S
GONDWANA
A

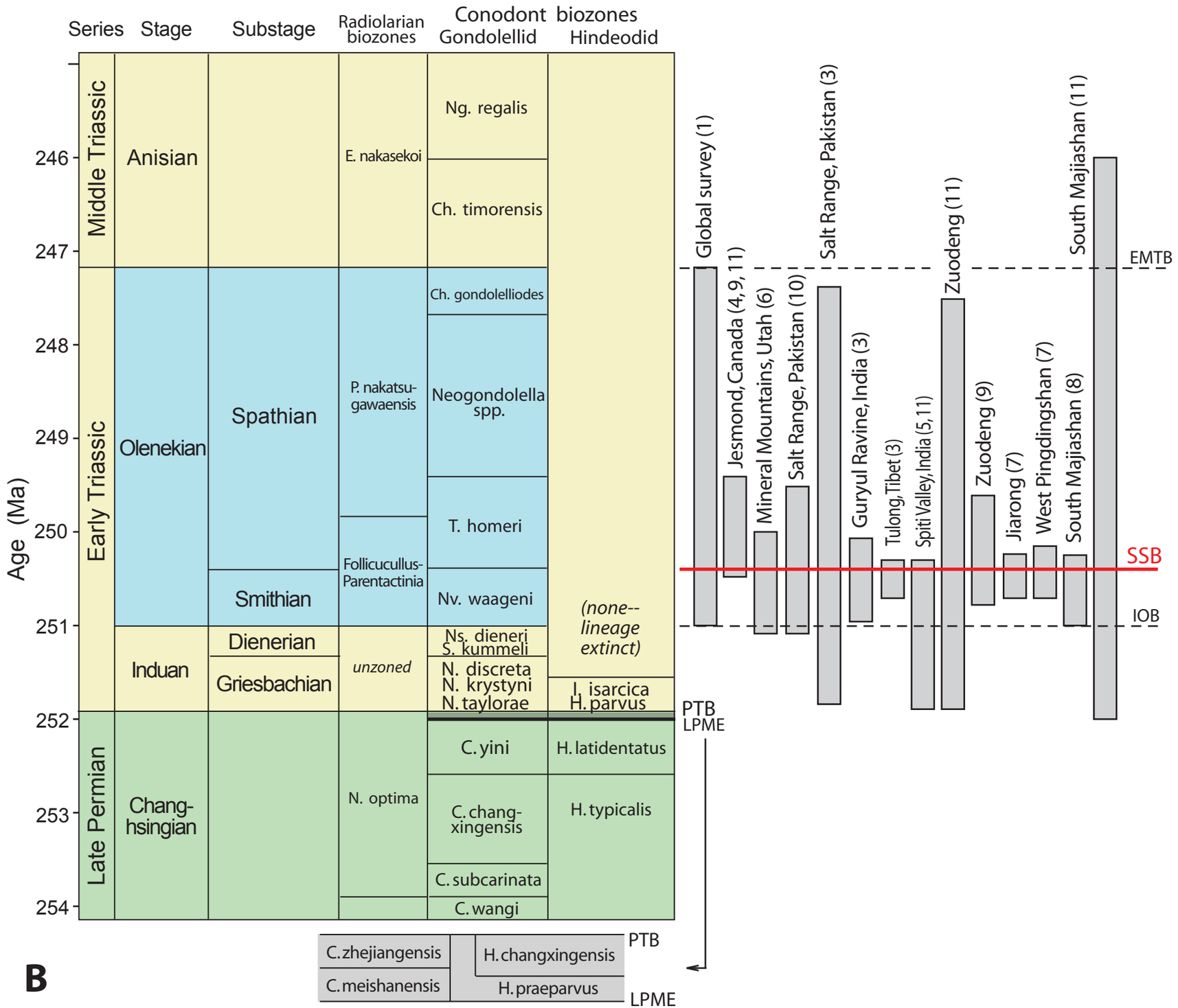
Series
Stage
Substage
Radiolarian biozones
Conodont biozones
Gondolellid
Hindeodid
Age (Ma)
246
247
248
249
250
251
252
253
254
Middle Triassic
Early Triassic
Late Permian
Anisian
Olenekian
Induan
Chang-hsingian
Spathian
Smithian
Dienerian
Griesbachian
E. nakasekoi
P. nakatsu-gawaensis
Follicucullus-Parentactinia
unzoned
N. optima
Ng. regalis
Ch. timorensis
Ch. gondolelliodes
Neogondolella spp.
T. homeri
Nv. waageni
Ns. dieneri
S. kummeli
N. discreta
N. krystyni
N. taylorae
C. yini
C. chang-xingensis
C. subcarinata
C. wangi
(none--lineage extinct)
I. isarcica
H. parvus
H. latidentatus
H. typicalis
PTB
LPME
C. zhejiangensis
C. meishanensis
H. changxingensis
H. praeparvus
PTB
LPME
B
Global survey (1)
Jesmond, Canada (4, 9, 11)
Mineral Mountains, Utah (6)
Salt Range, Pakistan (10)
Salt Range, Pakistan (3)
Guryul Ravine, India (3)
Tulong, Tibet (3)
Spiti Valley, India (5, 11)
Zuodeng (11)
Zuodeng (9)
Jiarong (7)
West Pingdingshan (7)
South Majiashan (8)
South Majiashan (11)
EMTB
SSB
IOB